Journal of Theoretical and Applied Physics (2020) 14:223–236
https://doi.org/10.1007/s40094-020-00381-6

RESEARCH

Anti-corrosion properties of stainless steel 304L coated with Mn-based thin film and annealed with nitrogen flux exposed to saline solution under various temperatures

Farzaneh Modiri[1] · **Hadi Savaloni**[2]

Received: 29 December 2019 / Accepted: 12 June 2020 / Published online: 24 June 2020
© Islamic Azad University 2020

Abstract
In this work the corrosion resistance of stainless steel 304L coated with Mn-based thin film and post annealed with flow of nitrogen at 723 K in 0.6 M NaCl solution is reported. The latter was performed at three different solution temperatures of 293 K, 313 K and 333 K. X-ray diffraction analysis was used to determine the crystallographical structure and phases of the annealed samples. Atomic force microscope and field emission scanning electron microscope were employed to determine the morphology of the surface of the samples. Corrosion behavior of the samples in the corroding media was studied by means of electrochemical impedance spectroscopy (EIS) and polarization analysis. Results showed that the sample investigated in the 0.6 M NaCl solution at 293 K temperature has the highest corrosion resistance than those studied at higher temperatures. The correctness of the EIS results was confirmed by Kramers–Kronig transformation, while fitting of the data (Nyquist and Bode diagrams) to suitable equivalent electrical circuits showed that the highest corrosion enhancement is achieved for the Mn-based/SS304L sample in the 0.6 M NaCl solution at 293 K temperature, resulting in a 90.57% corrosion inhibition enhancement factor (η%). Polarization measurements also showed that this sample has the lowest corrosion current density, lowest corrosion rate and highest corrosion potential with a 96% corrosion inhibition efficiency factor (PE%). Consistent results are achieved for EIS and polarization measurements which are then correlated with the nanostructure of the films using X-ray diffraction and atomic force microscope analyses.

Keywords Corrosion · Mn thin films · Potentiodynamic · Stainless steel 304L · Electrochemical · Impedance spectroscopy · Kramers–Kronig transformation

Introduction

Metals like plain-carbon steel, aluminum, copper, and their alloys have numerous applications in marine, aeronautic, industrial, and manufacturing sectors [1–5]. While these metals are valuable for their physical properties such as toughness and the high ratio of strength to weight, they are very vulnerable to corrosion under corrosive environments [6–9]. Therefore, the main reason for using stainless steels is their high resistance against corrosion [10, 11]. Properties such as resistance against corrosion, high strength, and favorable mechanical features have led to their application in numerous scientific and engineering fields including chemical and pharmaceutical industries, petrochemical industries, oil and gas lines, and marine constructions [12, 13]. Formation of a film on the surface of stainless steels improves their resistance against corrosion. On the other hand, the presence of Cl, Br, and I ions destroys this passive layer and results in pitting corrosion [14, 15]. Pitting corrosion occurs as small regions locally selected leading to formation of small cavities and pores [6]. In stainless metals, pitting corrosion occurs when the electrode potential exceeds a critical level (cavitation potential) [16, 17].

Boilers and water cooling systems are among the most important equipment made of stainless steels [18–20]. Increased temperature in this equipment can influence the rate of corrosion in steels. Generally, increase in the

✉ Hadi Savaloni
savaloni@khayam.ut.ac.ir

[1] Plasma Physics Research Center, Faculty of Sciences, Science and Research Branch, Islamic Azad University, Tehran, Iran

[2] School of Physics, College of Science, University of Tehran, North-Kargar Street, Tehran, Iran

temperature speeds up the oxidation and reduction reactions on the metal surface and as a result, corrosive ions have a better access to the surface and the density of corrosion current is increased [21]. Jian et al. [22] studied the effect of temperature on corrosion of 304 type stainless steel in a media containing NaCl and found that the passive layer was in its most stable condition up to 20 °C and the produced cavities were quickly recovered. However, with increasing the temperature to 40, 60, and 80 °C, the passive layer increasingly lost its stability and the vulnerability of the surface to corrosion increased. Moreover, they showed that the increase in the rate of corrosion is not the same in different temperature ranges and it is higher within the temperature range of 60–80 °C compared with that of 40–60 °C.

Various methods are proposed to improve resistance against pitting corrosion of stainless steels in the equipment used under temperatures higher than the ambient temperature. Coating is one of the most important methods proposed for this purpose [23–26]. In recent years, various coatings have been studied for the stainless steels submerged in the media containing NaCl and the effect of temperature on their corrosion rate has been analyzed. Zhang et al. [27] in their study on the 304 type stainless steel coated with a layer of hopeite conversion coating film and submerged in a 0.9% NaCl solution under various temperatures (45–85 °C) observed that despite significant enhancement of the corrosion resistance of the coated sample relative to that of uncoated one, increasing the corroding medium's temperature from 45 to 85 °C led to increase of corrosion rate by a factor of three. Mohammadloo et al. [28] found that with an increase in the temperature from 20 to 40 °C, the corrosion current density of the steel coated with a hexafluorozirconic-based conversion coating submerged in a 3.5% NaCl medium increased from about 5.11–11.31 μA/cm^2 which means the corrosion rate doubled with the raise in temperature.

Another important parameter to prevent pitting corrosion is the thickness of the coating. Chou et al. [29] coated 304 type stainless steel with TiN thin films of different thicknesses and studied their corrosion behavior in 5% NaCl solution. Their results showed that the minimum thickness required for the sample being resistance against pitting corrosion is 0.7 μm. Curkovic et al. [30] in their studies on the effect of the thickness of TiO_2 coating on the corrosion of 304 type stainless steel in 3% NaCl solution reported that increasing the thickness of the coating reduced pitting corrosion rate. Therefore, increasing the thickness of the coating can have some favorable influences on enhancement of pitting corrosion resistance of stainless steel. However, increased thickness may impose some limitations on the performance of the coated samples in practical applications. Therefore, achieving resistance to pitting corrosion through formation of a thin layer of coating on the samples can have an ideally promising perspective in practical applications.

The only work related to the temperature of the corroding medium on the corrosion of 304L type stainless steel is reported by Salih et al. [31] in which they did not coat the sample and studied the effect of temperature of NaCl and NaI solutions on the uncoated but polished 304L and 304 types stainless steel. Their results showed that both samples suffered from severe pitting corrosion at room temperature up to 50 °C.

The aim of this work is to study the influence of corroding medium (0.6 M (3.5%) NaCl solution) temperature on the 304L type stainless steel as deposited by 190 nm Mn-based (hereafter called Mn) thin film and subsequently annealed with flow of nitrogen to produce Mn-nitride. Generally, ceramic or organic coatings increase the corrosion resistance of a metallic substrate via three mechanisms: barrier protection, passivation of the substrate surface (inhibitive effect), and sacrificial protection (galvanic effect). Ceramic coatings can improve the corrosion resistance of a substrate by impeding the transport of aggressive species into the surface of the substrate due to their low permeability for the corrosive electrolyte. Therefore, barrier protection of Mn-based ceramic coating can be considered as the main mechanism for the corrosion resistance enhancement in this work. To the best of our knowledge at the time of submission of this manuscript this is the first report on corrosion of 304L type stainless steel in which this method of deposition is used. Corrosion behaviors of the produced samples are analyzed by electrochemical methods namely electrochemical impedance spectroscopy (EIS) and polarization measurement. The results of EIS and polarization measurements showed a possible corrosion inhibition enhancement factor ($\eta\% = 90.57\%$) and a corrosion inhibition efficiency factor (PE% = 96%), respectively for the sample measured at 293 K corroding medium temperature. Physical structure of the samples are obtained using atomic force microscopy (AFM) and field emission electron microscopy (EIS) while their crystallographic structure is obtained by means of X-ray diffraction analysis (XRD). Kramers–Kronig transformation analysis of the results confirmed the EIS data [32, 33].

Experimental details

The 304L type stainless steel of ($21 \times 21 \times 1$ mm^3) was employed as substrate. X-ray fluorescence (XRF) analysis and CS-2000 device were used to determine the chemical composition and carbon content of the samples (Table 1).

The as received 304L type stainless steel (SS304L) was covered with a polyethylene sheet to prevent oxidation and mechanical damage. The protective sheet was removed by immersing the samples in ethanol for several days before they were thoroughly cleaned with an ultrasonic device in heated acetone (CH_3COCH_3) and then in

Table 1 Chemical composition of the 304L type stainless steel

Sample	Element (wt%)					
SS304L	V	Cr	Co	Ni	Mo	C
	0.061	14.293	0.202	5.699	0.087	0.024

ethanol (C_2H_5OH) for at least 20 min. Mn (99.98%) with a film thickness of 190 nm was deposited on the SS304L substrates by electron beam using (Model E19A3 Edwards, England) with a base pressure of 5×10^{-7} mbar and at room temperature. Mn deposition rate and thickness was measured by a quartz crystal controller (Sigma Instruments, SQM-160, USA) placed near the substrate. A deposition rate of 0.6 $Å s^{-1}$ was used.

The Mn/SS304L samples were then annealed at the constant temperature of 723 K with a 300 sccm flow of N_2 gas (99.999%) in a horizontal tube furnace (Exciton, 1200–30/6, T.H, Iran). The furnace was equipped with a temperature controller (Shinko PCD 33A) programmable with 9 different programs of 9 stages and the maximum temperature of 1200 °C. The annealing of the Mn samples took place in three stages as: (1) the samples were heated to a temperature of 723 K for 2 h. (2) They were, together with the nitrogen flux, kept at this temperature for 6 h. (3) They were allowed to cool down for 10–12 h until they reached room temperature.

A phenomenon referred as "sensitization" occurs at temperatures higher than 700 K to stainless steel where Cr at their grain boundaries reacts with carbon content leading to formation of chromium carbide. Consequently, reduced chromium contents along these regions increases the probability of grain boundary corrosion.

Crystallography and crystallite size (coherently diffracting domains) information were obtained by means of XRD analysis (Stoe STADI-MP diffractometer) with Cuk_α source, step size of 0.02° and count time of 1.0 s per step, and energy 30 keV. Surface morphology, roughness of each sample, and the grain size were obtained from AFM analysis (NT-MDT Scanning Probe Microscope, TS 150) and FESEM (FEI NOVA NanoSEM450).

A potentiostat coupled with a PC (Ivium, De Zaale 11, 5612 AJ Eindhoven, Netherlands) was used for EIS measurements with reference to the open circuit potential (OCP) within 0.01 Hz–100 kHz, an amplitude of 10 mV, and on 1 cm^2 surface area of the samples. An Ag/AgCl (saturated KCl, + 0.197 V vs. standard hydrogen electrode potential) electrode was used as reference and a Pt electrode served as the auxiliary electrode. The test sample—the working electrode—was mounted on a polyamide (inert) fixture to get an electrical contact with no unwanted effects. Samples were immersed in the 0.6 M NaCl (corroding medium) and the OCP measurement was performed prior to the EIS test to make sure of the stability of the system for at least 50 min. The EIS measurements were performed at the three designated temperatures (293, 313 and 333 K) after achieving equilibrium at each of these temperatures. The temperature of the corroding medium was kept constant throughout of each electrochemical impedance spectroscopy and polarization analysis. EIS data were fitted by corresponding equivalent electric circuits using ZView software version 3.1 c.

The corrosion resistances of the samples were precisely analyzed and compared based on the impedance, phase-Bode, and the Kramers–Kronig diagrams.

In this measurement set up, the polarization potential was applied to the sample by a copper wire attached to the back side of the sample which was mounted on the polyamide fixture. Also, an Ag/AgCl and a Pt electrode were considered as the reference and the counter electrode, respectively. The potential was swept with a rate of 1 mV/s to deal with a span of about 2 V (within − 1 V and + 1 V) for each sample, starting from -1 V vs. OCP. The electrochemical tests were repeated three times for each sample to ensure the validity of the test results.

The rate of—and resistance to—corrosion for each sample were determined by calculating the corrosion current density, i_{corr}, and the corrosion potential, E_{corr} using Stern–Geary equation:

$i = i_{corr}\left\{\exp\left[b_a\left(E - E_{corr}\right)\right] - \exp\left[b_c\left(E - E_{corr}\right)\right]\right\}$ and by fitting the polarization curve for each sample to the anodic and cathodic branches, using MATLAB.

Results and discussions

AFM analysis

Results of surface morphology analysis using an atomic force microscope (AFM) and also the relevant measurements including grain size (D_{AFM}), average surface roughness (R_{ave}), and the root mean square of surface roughness (R_{rms}) of 1 μm^2 of each stainless steel sample (SS304L, Mn/SS304L, and MnNx/SS304L) are shown in Fig. 1 and Table 2, respectively. Deposition of Mn on SS304L produced an almost uniform grain distribution on the substrate surface with increased grain size and reduced surface roughness relative to the bare SS304L substrate. However, after annealing of the Mn/SS304L sample with flow of nitrogen at 723 K temperature the surface roughness increased and the grain size is decreased. These changes can be related to diffusion effect at this annealing temperature and the solubility

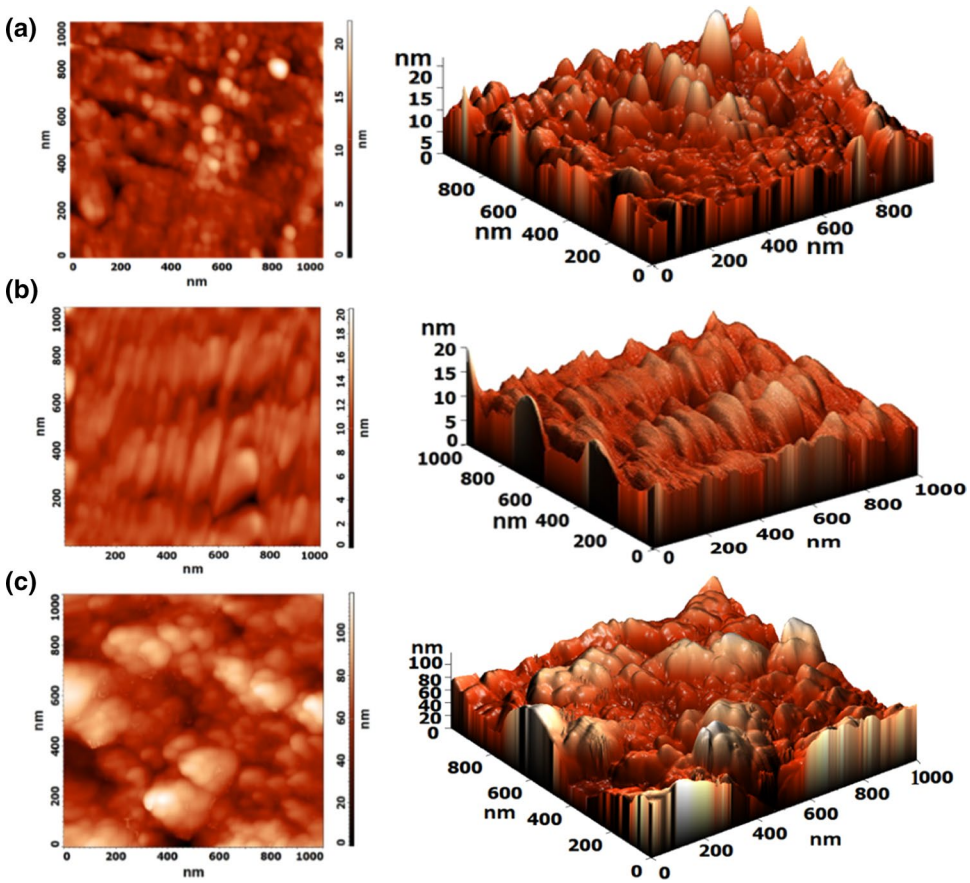

Fig. 1 2D and 3D AFM images of **a** SS304L, **b** Mn/SS304L and **c** MnN_x/SS304L

Table 2 Grain size (D_{AFM}), average surface roughness (R_{ave}), and the root mean square surface roughness (R_{rms}) of the samples produced in this work obtained from AFM analysis

Sample	R_{rms} (nm)	R_{ave} (nm)	D_{AFM} (nm)
SS304L	2.33	1.75	53.85
Mn/SS304L	1.49	1.11	108.72
MnN_x/SS304L	16.26	12.71	84.40

of nitrogen in the Mn coating which act opposite to each other. Solubility/penetration of nitrogen molecules can break up the Mn grains to smaller ones [34] while diffusion effect leads to larger grains being formed. The competition between these two processes has resulted in the formation of the MnN_x/SS304L sample in this work shown in Fig. 1c.

XRD analysis

Figure 2 presents the XRD patterns of the samples produced in this work and analyzed using the standard JCPDS cards. The result for SS304L shows peaks at angles 44.426, 51.581, 75.477, and 91.432 degrees, corresponding to γ—Fe(111), γ—Fe(200), γ—Fe(220), and γ—Fe(311), respectively, in accordance with the JCPDS card No: (00-003-0397). For

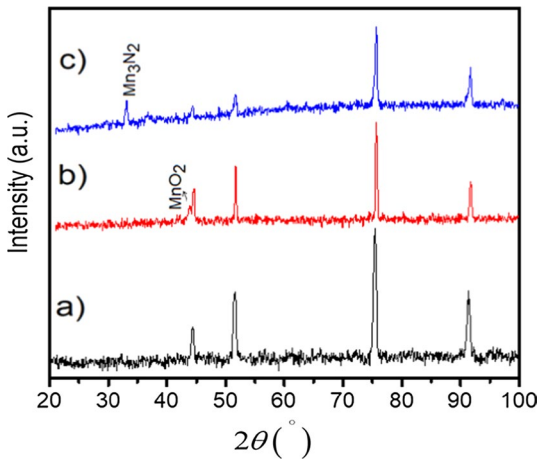

Fig. 2 XRD patterns of the samples produced in this work: **a** SS304L, **b** Mn/SS304L and **c** MnN_x/SS304L

the Mn/SS304L, in addition to the four peaks observed for SS304L sample a peak is appeared at 43.674° which belongs to MnO_2 (140) according to JCPDS card No: (00-005-0600). The reason for oxidation of Mn film in this sample should be the oxide formation of the source material during pumping of the PVD system until the pressure of the system reached 5×10^{-7} mbar and also during deposition at this pressure as

well as being exposed to air after deposition for performing the XRD measurement.

As Fig. 2b suggests, due to deposition of 190 nm Mn on the SS304L substrate, the magnitudes of peaks related to SS304L are reduced compared with Fig. 2a. In case of MnN_x/SS304L, again the XRD pattern shows the SS304L four peaks with further decrease of their intensity and formation of Mn_3N_2(112) diffraction line at 33.106° in accordance with the JCPDS card No: (01-081-0299) confirming the Mn-nitride formation.

FESEM and EDS analyses

Surface and cross-section FESEM images of Mn/SS304L sample before annealing process are given in Fig. 3. There are some lined cracks on the surface of this sample (10 µm scale image) while finer cracks/kink scan also be observed on the 1 µm scale image (inset). The inset of the cross-section image clearly shows both the as deposited film thickness (i.e., 190 nm) and the tapered structure consistent with the structure zone model (SZM) [35–39].

To confirm the XRD results (Fig. 2), [35] discussed in the preceding section the energy dispersive spectroscopy (EDS) analysis was carried out on the Mn/SS304L sample (Fig. 3c and Table 3). The high intensity peaks for Mn and oxygen clearly confirm the formation of Mn-oxide.

Electrochemical polarization analysis

Polarization curves obtained from the measurements on all samples produced in this work are given in Fig. 4.

The polarization curve for SS304L shows that the passive potential and passive current density for this sample are ($E_P = -0.125$ V) and ($J_P = -1.1$ mA/cm^2), respectively which because of the formation of an oxidized layer, as with a chromium oxide layer on metals [40], the speed of corrosion reactions are reduced in the region [41, 42]. When the anodic polarization increased to 0.105 V, this layer breaks and the corrosion reactions rise. This makes the system enter a transpassive phase and the oxidization starts on the surface layer. In case of Mn/SS304L sample, the passive potential and transpassive potential are 0.250 V and 0.603 V, respectively. Since the potential range in which Mn/SS304L is in

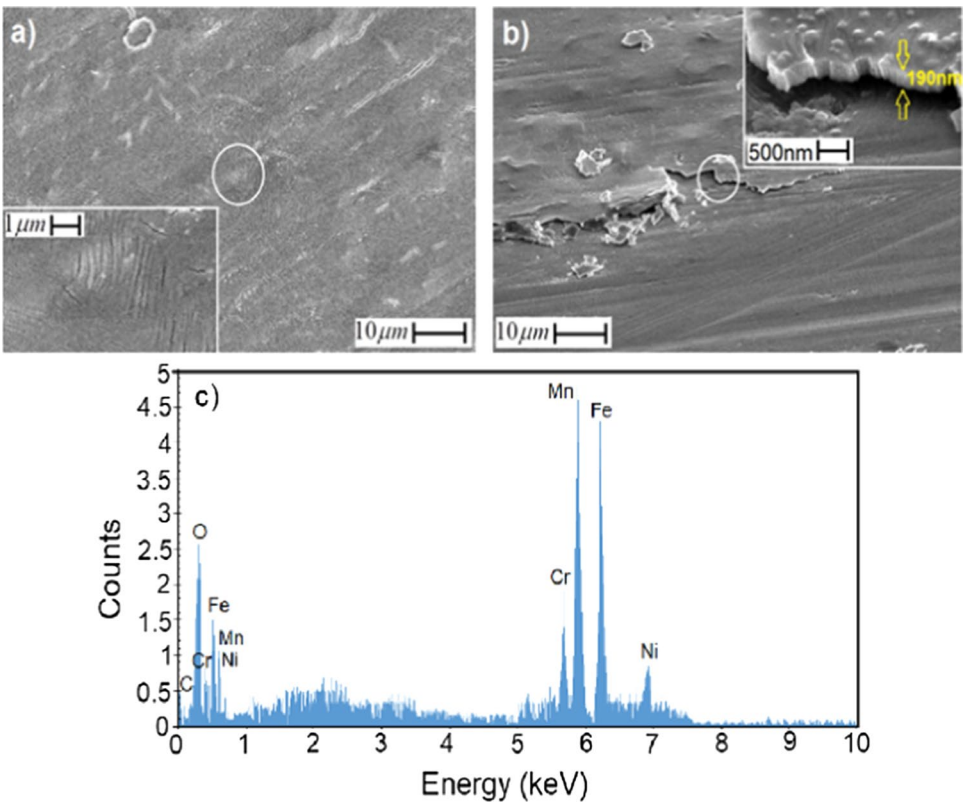

Fig. 3 FESEM images of Mn/SS304L sample before annealing process: **a** surface, **b** cross-section, **c** EDS spectrum

Table 3 EDS elemental analysis (wt%) for Mn/SS304L sample

Sample	Fe	Mn	Cr	C	Ni	O
Mn/SS304L	43.76	38.64	10.07	0.56	3.52	3.45

the passive state is wider than that for SS304L sample, it can be concluded that the surface of the former sample is more stable than the latter sample which can be due to deposition of Mn on SS304L.

After annealing, the corrosion passivation for MnN_x(293 K)/SS304L and MnN_x(313 K)/SS304L are 0.227 V and for MnN_x(333 K)/SS304L, is 0.360 V. The transpassive region was measured outside the potential range. Anodic branches in all three samples after annealing were similar because of the oxidized nature of the coatings; however, the cathodic branch of MnN_x(293 K)/SS304L sample is at a lower current density compared to other samples. The difference in current density, corrosion potential, and Tafel anodic and cathodic slopes are attributed to the variations in surface morphology and phase composition of the coatings. Therefore, regarding the direct relationship between current density and corrosion speed, MnN_x(293 K)/SS304L sample has shown the highest level of corrosion resistance.

The temperature of the corroding solution clearly influences cathodic reactions and works in favor of the kinetics present in the corrosion reaction. The temperature also increases the anodic collapse of the metal as the intensity of anodic currents also increases at higher temperatures [43, 44].

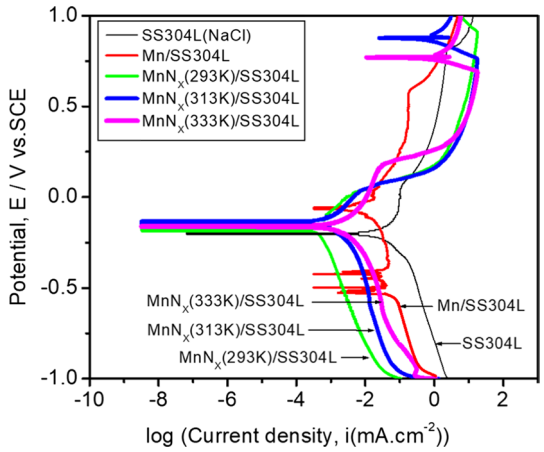

Fig. 4 Polarization curves for SS304L, Mn/SS304L, MnN_x(293 K)/SS304L, MnN_x(313 K)/SS304L, and MnN_x (333 K)/SS304L

$$\text{UsingStern} - \text{Geary equation}: i = i_{\text{corr}}\left\{\exp\left[b_a\left(E - E_{\text{corr}}\right)\right] - \exp\left[b_c\left(E - E_{\text{corr}}\right)\right]\right\}$$

fitting process was carried out with a precision of 98%. Potential E and current density i are the known values in the equation that are determined based on its fitting range. Thus, E_{corr}, i_{corr}, b_a, and b_c in each sample are obtained based on the fitting curve. Corrosion potential E_{corr} of each sample was measured based on the polarization curve. Also, the fitting ranges were selected using MATLAB between 10 V lower and 50 V higher than E_{corr} for the anodic branch and between 10 V higher and 50 V lower than the corrosion potential for the cathodic branch. Therefore, the best fittings for anodic and cathodic branches were acceptable solutions [45].

The corrosion inhibition efficiency factor is defined as:

$$\text{PE}\% = \frac{i^0_{\text{corr}} - i^{\text{c}}_{\text{corr}}}{i^0_{\text{corr}}} \times 100, \tag{1}$$

where i^0_{corr} is the corrosion current density (anodic or cathodic) for the substrate (SS304L) an $i^{\text{c}}_{\text{corr}}$ is the corrosion current density (anodic or cathodic) for the coated samples.

The fittings results for the SS304L, Mn/SS304L, MnN_x(293 K)/SS304L, MnN_x(313 K)/SS304L, and MnN_x(333)/SS304L samples with the polarization curves and the relevant values for the anodic and cathodic branches in 0.6 M NaCl solution at different temperatures are separately shown in Tables 4 and 5 where it is possible to determine the stability and corrosion properties of each surface based on the corresponding values of the current density and the corrosion inhibition efficiency factor.

Moreover, the porosity of the sample (P) is obtained based on Eq. (2):

$$P = \frac{R_{\text{ps}}}{R_{\text{p}}} \times 10^{-\left(\frac{\Delta E_{\text{corr}}}{b_{\text{a}}}\right)}, \tag{2}$$

where R_{ps},R_{p}, ΔE_{corr}, and b_{a} are the polarization resistance of the sample without coating, the polarization resistance of the sample with coating, difference in corrosion potential

Table 4 Corrosion parameters of the anodic branch of the polarization curves for the samples produced in this work in 0.6 M NaCl

Sample	Anodic					
	J_{corr} (mA/cm^2)	E_{corr} (V_{SCE})	b_{a} (V^{-1})	b_{c} (V^{-1})	PE%	P
SS304L	5.270	− 0.200	0.354	0.164	–	–
Mn(293 K)/SS304L	4.855	− 0.528	59.800	57.200	7.87	0.115
MnN_x(293 K)/SS304L	0.200	− 0.194	0.714	0.685	96.20	0.328
MnN_x(313 K)/SS304L	0.455	− 0.139	0.649	0.585	91.36	0.497
MnN_x(333 K)/SS304L	0.794	− 0.161	0.437	0.360	84.93	0.490

Table 5 Corrosion parameters of the cathodic branch of the polarization curves for the samples produced in this work in 0.6 M NaCl

Sample	Catodic				
	J_{corr} (mA/cm^2)	E_{corr} (V_{SCE})	b_a (V^{-1})	b_c (V^{-1})	PE%
SS304L	6.300	− 0.200	− 0.065	0.223	–
Mn(293 K)/SS304L	3.521	− 0.528	− 63.450	− 64.03	44.11
MnN_x(293 K)/SS304L	0.240	− 0.192	0.615	0.572	96.19
MnN_x(313 K)/SS304L	0.420	− 0.139	0.693	0.139	93.33
MnN_x(333 K)/SS304L	0.774	− 0.161	0.690	0.614	87.71

between the coated sample and the sample without coating, and Tafel slope of the anodic branch of the sample without coating.

Results in both of these Tables show that best performance against corrosion is achieved for the MnN_x(293 K)/SS304L sample (i.e., least value for the corrosion current density and highest PE% value) while the corrosion current density is increased and the PE% value decreased with increasing the corroding medium temperature. This can be related to the increase of porosity (Table 4) and the anodic reaction speed [41, 42].

It is usually expected that the lowest corrosion current density associated with highest corrosion potential, while this is not the case in all cases and varies with the different complex parameters involved in the system under examination. The small deviation from this is observed in our values for corrosion potential (Tables 4, 5) which can be assumed negligible because the current density is the critical parameter for evaluating the corrosion resistance of materials, and the lower this value, the better corrosion resistance (considering that corrosion potential does not change significantly) (Tables 4, 5) [46]. The E_{corr}, values cannot give any specific information about the corrosion trend [47]. On the other hand, there may have formed a passive layer on the surface of the sample at annealing temperature of 293 K [48].

EIS analysis

A common mechanism in corrosion is the atomic, molecular, or ionic transmission that occurs in the interface of the substance-environment. The mass transmission through the interface with the environment can be conceptualized as an electrochemical, chemical, or physical property. Since electrochemical corrosion involves releasing ions into the environment and movement of electrons in the substance, this mechanism can take place only when the environment contains ions or electric conductive compounds.

The most important electrochemical mechanism is the simple corrosion in aquatic medium where atoms at the metal surface are released into the solution in the form of ions and the metal electrons are transferred to locations where they are consumed by the particles in contact with the metal, maintaining the reaction process. The ions form a layer with positive charge on the metal surface while electrons form a layer or negative charge in the metal. This phenomenon creates an extra electrical layer which, as an electric force prevents further dissolution of the metal. This extra layer which is formed as a result of the electrical charge separation is similar to a charged capacitance. A difference in electric potential is created between the two layers with an electromotor force (EMF) based on Eq. (3):

$$Q = CV, \tag{3}$$

where Q is the electric charge, C is the capacity that determines the characteristics of the electrode, and V is the resulting EMF in volt. Here, V is the absolute electric potential of the electrode relative to a reference electrode. Although there is electrical resistance at the solution-metal interface but there is an electric current transfer through it too. Therefore, the system can be depicted as an electric circuit consisting of a capacitance parallel with a resistance (R_F) called Faraday resistance which is not ohmic and poses resistance against the passage of the probable current. Consequently, when the electrical charge changes by dQ the electrical potential should change by dV, and the differential electric capacitance can be defined as:

$$C_{dl} = \frac{dQ}{dV}. \tag{4}$$

This parameter shows the capacity of an interface for storing electrical charge. Therefore, C_{dl} and R_F are the two main characteristics of the system.

The complex impedance diagram, i.e. the imaginary part of the impedance is a function of its real part, in the form of a semi-circle. However, in most cases, the impedance semi-circles resulting from the experimental findings are in the form of compressed semi-circles. Therefore, the constant phase element (CPE) must be used instead of an ideal capacitor. The impedance of this electrical element with a constant phase is determined using Eq. (5):

$$Z_{CPE} = \left[Y_0(j\omega)^n\right]^{-1}, \tag{5}$$

where $\omega\left(\text{rads}^{-1}\right)$ is the angular frequency, Y_0 is the constant value of CPE or admittance, j is the imaginary unit, and n is the surface uniformity coefficient. For a smooth surface, n

may be assigned as unity, while rough surfaces have lower values. A Warburg impedance is usually used instead of a CPE when $n = 0.5$.

The relationship between Y_0 and C_{dl} is obtained from Eq. (6):

$$C_{dl} = Y_0 \left(\omega_{max}\right)^{n-1}, \tag{6}$$

where ω_{max} is the angular frequency of the point where the imaginary component of the impedance is maximum [49, 50].

The corrosion inhibition enhancement factor (η) is defined as:

$$\eta(\%) = \frac{R_P(\text{film}) - R_P}{R_P(\text{film})} \times 100, \tag{7}$$

where R_P and R_P(film) are polarization resistances of uncoated SS304L and treated Mn/SS304L samples respectively.

Formation of a tiny capacitance loop (semi-circle) showing resistance in the coating is related to a new interface between the metal and electrolyte which is caused by the penetration of the electrolyte through the porosity and surface openings of the coating. Besides, a new electric double layer is created between the metal and electrolyte at some regions of the metal surface and as a result, another capacitance loop (semi-circle) is formed at lower frequencies showing resistance of charge transfer. Increased diameter of the semi-circle indicates improved resistance against corrosion and is a criterion for measuring the corrosion resistance of the system.

In Fig. 5 the large diameter of the semi-circle for MnN_x(293)/SS304L sample indicates the stability of this sample compared to the other samples. As seen, sample MnN_x(313)/SS304L at lower frequencies still has not achieved the resistant state although regarding the values obtained from the polarization graph and considering increased speed of corrosion with an increase in the temperature, the sample's resistance is expected to reduce in comparison with MnN_x(293)/SS304L sample. Therefore, based on the study [51], this can be attributed to the minimum depression of C_{dl} in the sample.

The impedance spectrum was modeled using Zview software with a circuit composed of resistors and a capacitance. According to Fig. 6a, the equivalent circuit that best fits SS304L sample in 0.6 M NaCl solution, has one time constant. In the graphs with a time constant there is only one interface between the electrolyte and the sample. In this circuit, R_S, C_{dl}, and R_{ct} are the resistance of the solution, the capacitance of the double layer of solution-substrate interface, and the resistance of the charge transfer in the solution-substrate interface, respectively.

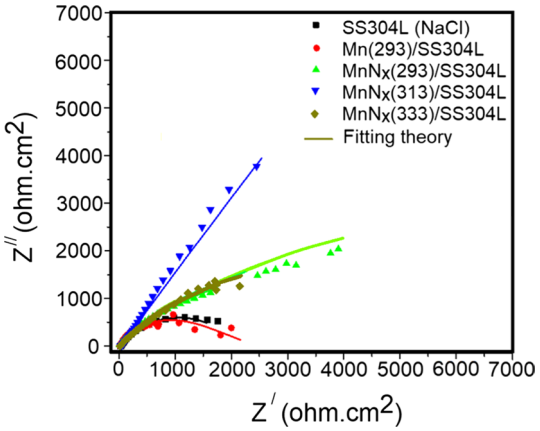

Fig. 5 Nyquist curves and fits based on the equivalent circuits for modeling the impedance data, in 0.6 M NaCl solution at different temperatures

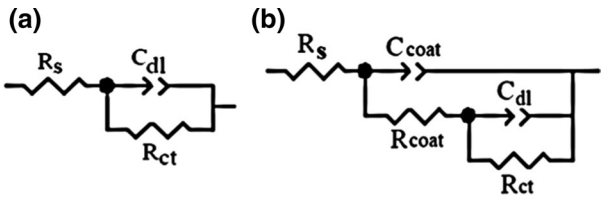

Fig. 6 The equivalent electrical circuit corresponding to **a** SS304Lwith a single time constant and **b** Mn(293 K)/SS304L, MnN_x(293 K)/SS304L, MnN_x(313 K)/SS304L and MnN_x(333 K)/SS304L with two time constants

As Fig. 6b shows the equivalent circuit that corresponds to Mn(293)/SS304L, MnN_x(293)/SS304L, MnN_x(313)/SS304L and MnN_x(333)/SS304L samples have two time constants. In this circuit, R_S, C_{dl}, R_{ct}, C_{coat} and R_{coat} are resistance of the solution, capacitance of the solution-substrate interface double layer, resistance of load transfer in the solution-substrate interface double layer, capacitance of the solution-Mn coating interface double layer, and the resistance of the coating layer resulted from the pores and defects, respectively.

Comparison of the values for the resistance of the coatings deposited on the substrates, R_{coat}, it can be deduced that the porous coating because of its heterogeneous structure and non-adhesion nature of the coating-substrate interface has a negligible resistance. Therefore, the main part of the resistance on the surface of the samples coated with manganese and manganese nitrate is related to the compressed internal layer which acts as a shield against the corrosive medium and improves resistance against corrosion in the sample.

Since the capacitance of the double layer depends on the value of the electric charge on the surface, lower values of C_{dl} show lower charge density. The Electrochemical parameters obtained from simulation procedure using Zview

program for all the samples examined in this work are given in Table 6.

The more precise analysis may be obtained from the Bode and Phase diagrams. Generally, the time constant at high frequencies is related to the presence of pores and defects in the coating of the substrate while at lower frequencies it is attributed to the metal-electrolyte interface [52–55]. Analysis of Bode and Phase diagrams based on the number of time constants (peaks) and also the capacitance and resistance regions. Results are given in Fig. 7. As Table 7 suggests, the

Table 6 Electrochemical parameters of uncoated SS304L and Mn/SS304L sample and Mn/SS304L samples annealed with flow of nitrogen and subjected to corrosion test in 0.6 M NaCl solution at different temperatures, obtained from simulation procedure using Zview program

Sample (NaCl)	R_s ohm cm^2	C_{coat}/ohm/cm^2 s	n_1	R_{coat} ohm cm^2	C_{dl}/ohm/cm^2 s	n_2	R_{ct} ohm cm^2	R_{tot}	η(%)
SS304L	33.28	–	–	–	1.04×10^{-3}	0.66	2017	2050.28	–
Mn(293 K)/SS304L	10.27	2.1×10^{-4}	0.78	12.67	1.09×10^{-3}	0.72	2100	2122.94	4.52
MnN_x(293 K)/SS304L	23.09	2.5×10^{-6}	0.43	24.87	1.1×10^{-5}	0.38	21,370	21,394.87	90.57
MnN_x(313 K)/SS304L	10.14	2.2×10^{-6}	0.72	27.56	1.4×10^{-3}	0.51	20,000	20,027.56	89.92
MnN_x(333 K)/SS304L	23.12	2.2×10^{-6}	0.76	15.09	1.5×10^{-3}	0.59	8300	8315.09	75.74

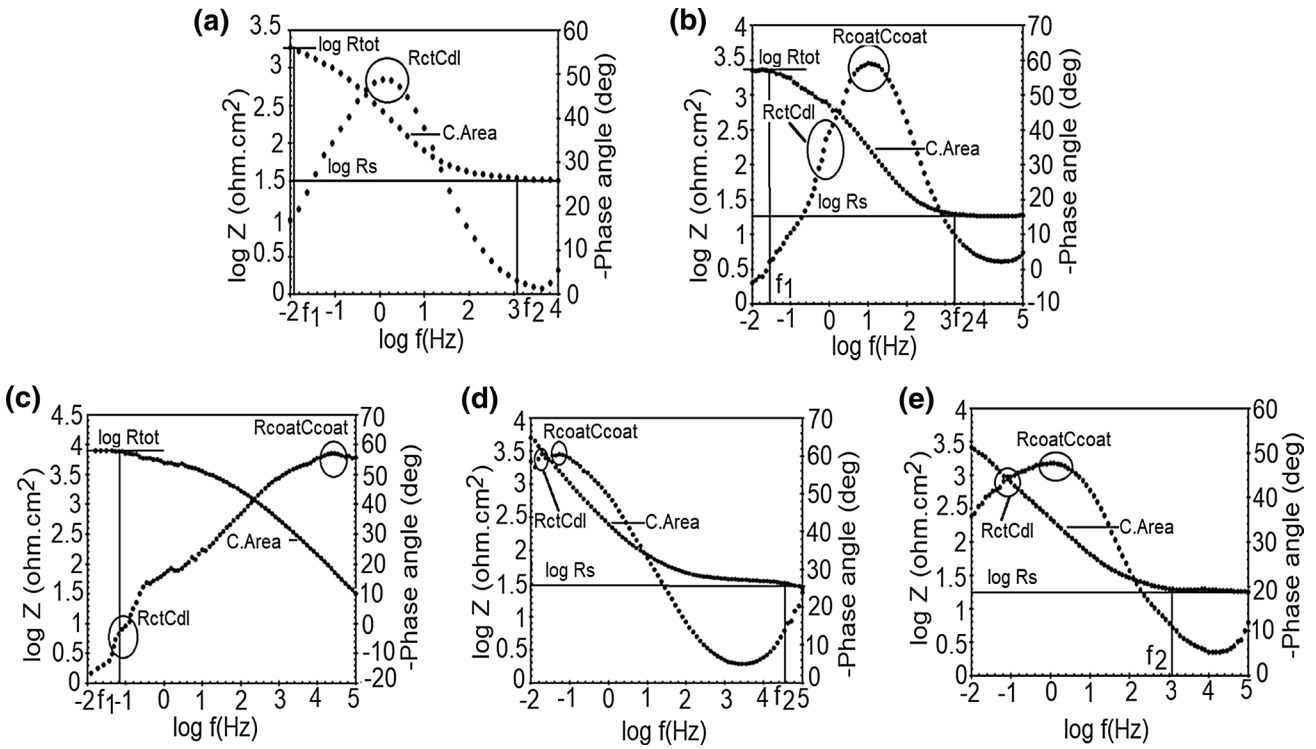

Fig. 7 Bode and phase diagrams for the samples **a** SS304L, **b** Mn(293)/SS304L, **c** MnN_x(293)/SS304L, **d** MnN_x(313)/SS304L and **e** MnN_x(333)/SS304L in a 0.6 M NaCl elctrolyte at different temperatures

Table 7 Resistances of the samples from the Bode diagrams and their comparison with those in Table 6

Sample	Log($R_{s+}R_{ct}$) ohm cm^2 Log($R_{s+}R_{ct}$) ohm cm^2	$R_{s+}R_{ct}$ ohm cm^2	R_{tot} ohm cm^2
SS304L	3.30	1995.26	2050.28
Mn(293 K)/SS304L	3.35	2238.72	2122.94
MnN_x(293 K)/SS304L	3.90	7943.28	6422.96
MnN_x(313 K)/SS304L	3.70	5011.87	6037.70
MnN_x(333 K)/SS304L	3.40	2511.88	5338.12

results of Bode and Phase diagrams are in good agreement with Nyquist curves and the difference in the values obtained for MnN_x(313 K)/SS304L and MnN_x(333 K)/SS304L is an indication that the Bode diagram at low frequencies is still in a capacitance state and has not reached the resistance state.

Kramers–Kronig transformation

It is imperative to verify the trustworthiness of the impedance data before analyzing and modeling the experimental results. A common mathematical approach to verification of these data is Kramers–Kronig transformations [56, 57]. The obtained impedance is verified provided that the following conditions are met:

- *Linearity* The obtained impedance should not vary with the ½ of the value of AC signal amplitude.
- *Causality* The system's response must be determined based on the disturbance of the applied potential and must be related to the input values only.
- *Stability* Stability of a system is determined with reference to its response to the system inputs. When an external force is applied to a stable system, removing the force returns the system to its original state.
- *Finiteness* The real and imaginary components of the impedance should be finite in all frequency ranges $0 < \omega < \infty$.

Generally, in Kramers–Kronig transformations Eqs. (9) and (10) are used to calculate the real and imaginary components of the experimental data on the electrochemical impedance [58–61].

$$Z'(\omega) = Z'(\infty) + \frac{2}{\pi}\int_0^\infty \frac{xZ''(x) - \omega Z''(\omega)}{x^2 - \omega^2}\mathrm{d}x \tag{9}$$

$$Z''(\omega) = -\left(\frac{2\omega}{\pi}\right)\int_0^\infty \frac{Z'(x) - Z'(\omega)}{x^2 - \omega^2}\mathrm{d}x. \tag{10}$$

Figure 8 shows the fitting of Kramers–Kronig transformations on Nyquist curves for all samples considering both "real to imaginary" and "imaginary to real" parts. It can be seen that good fit is obtained for all the samples which provides conditions to obtain the value of the real impedance for these samples.

FESEM analysis of samples after corrosion

Figure 9 depicts the FESEM images of the samples after corrosion test. Large cracks at grain boundaries of the un-annealed sample (Mn/SS304L) may be attributed to the possible defects in these regions. Corrosion started from these sites growing along the grain boundary. Moreover,

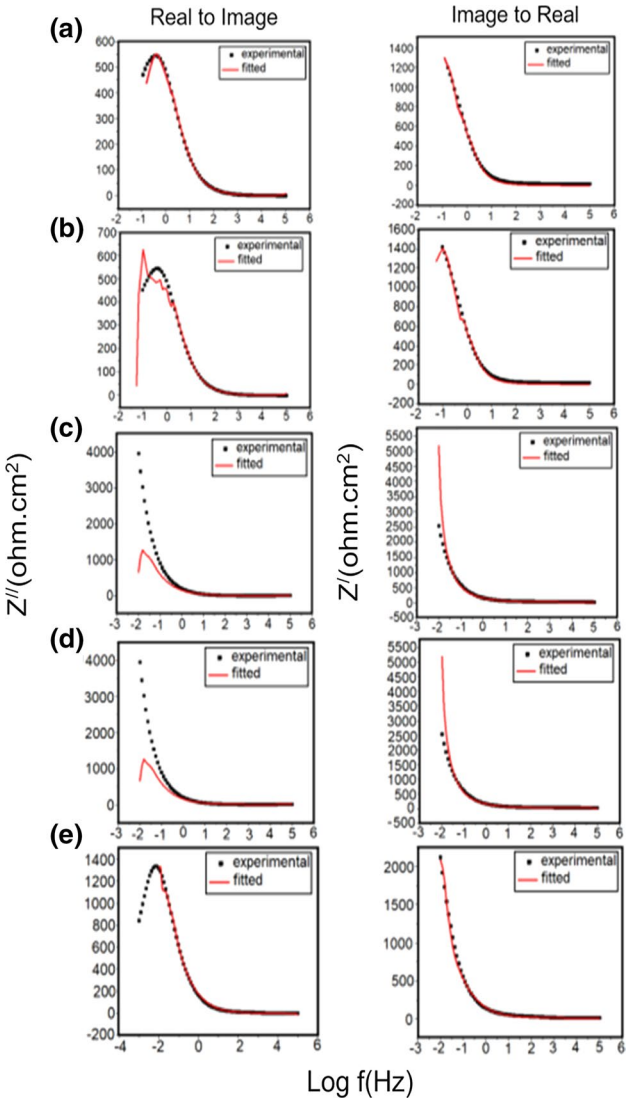

Fig. 8 Kramers–Kronig transformation of the real and imaginary elements of impedance for uncoated **a** 304L, **b** Mn(293)/SS304L, **c** MnN_x(293)/SS304L, **d** MnN_x(313)/SS304L and **e** MnN_x(333)/SS304L samples

the grain surfaces are characterized in terms of hillock patterns which may be resulted from corrosion at the porous structure of the deposited layer (see the tapered structure in Fig. 3). This is observed in the inset image in Fig. 9a. When the annealed sample at 723 K was analyzed in the corroding medium at 293 K (MnN_x(293 K)/SS304L) (Fig. 9b, almost no cracks (or cracks with much narrower width than that in the un-annealed sample (Fig. 9a) were found on the surface of the sample during corrosion test. On the other hand, a more uniform surface was observed which shows improved resistance to corrosion at 293 K corroding medium temperature (MnN_x(293 K)/SS304L) (Fig. 9b).Cracks started to emerge and uniformity of the surface decreased at 313 K and 333 K corroding medium

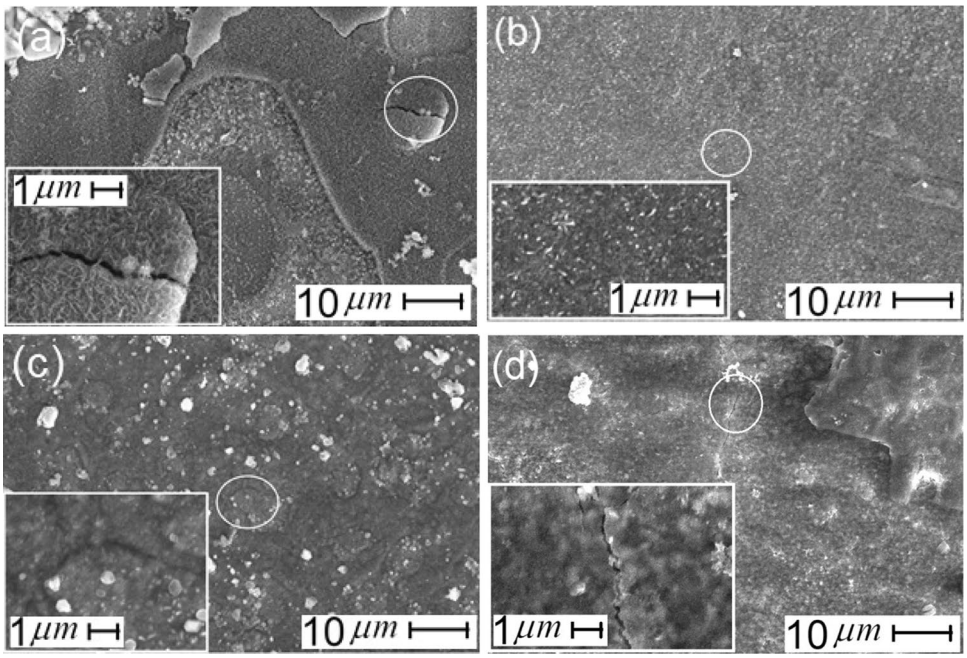

Fig. 9 SEM micrographs for **a** Mn/SS304L, **b** MnN_x(293 K)/SS304L, **c** MnN_x(313 K)/SS304L, and **d** MnN_x(333 K)/SS304L after corrosion in 0.6 M NaCl solution

temperatures((MnN_x(313)/SS304L) and (MnN_x(333)/SS304L) (Fig. 9c, d). Findings of the FESEM analysis are consistent with those obtained from electrochemical analysis discussed in the preceding sections.

Anti-corrosion mechanism of the Mn-nitride coatings

As mentioned in the introduction (Sect. 1) three mechanisms of inhibitive effect, galvanic (sacrificial) protection and barrier protection [50, 62] may be involved in the enhancement of corrosion resistance of ceramic (metallic nitrides/oxides). In the latter mechanism, the low permeability of the coating leads to the prevention of direct contact between the corrosive electrolyte and the electrode surface. Figure 10 shows the schematic of the protection mechanism of the Mn-nitride coatings.

As is depicted in Fig. 10a, iron atoms on the surface of steel substrate react with the chlorine ions dissolved in the corrosive electrolyte and release into the electrolyte as iron chloride resulting in pitting corrosion. The production of the latter reaction ($FeCl_2$) reacts with water molecules and convert to rust ($Fe(OH)_2$) and HCl. The decrease of pH inside the pits (due to the production of HCl in the latter reaction) causes further acceleration of the corrosion process. By applying the Mn-nitride ceramic coating on the stainless steel substrate a compact barrier formed against the corrosive species (i.e., chlorine ions), and so the substrate is protected by coating through barrier protection mechanism. Considering the fact that the barrier mechanism mainly depends on the permeability of the coating, the presence of micro cracks on the thin film leads to a decrease in the anti-corrosion performance of the system. Therefore, as seen in Fig. 9, the formation of

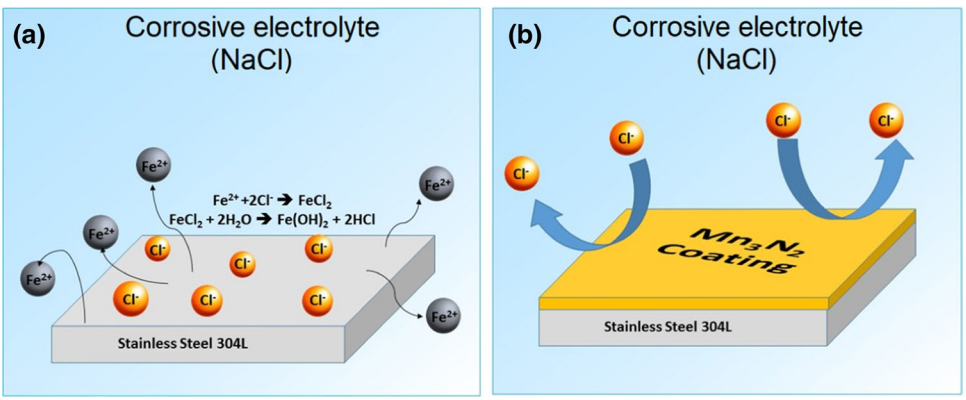

Fig. 10 Schematics of **a** corrosion reactions of stainless steel in Cl^- containing corrosive solution and **b** anti-corrosion performance of the manganese nitride coating on the stainless steel substrate

micro cracks on the Mn-nitride thin films by increasing the electrolyte temperature can lead to a negative effect on the anti-corrosion performance of the coating.

Summary and conclusions

1. The findings of XRD, AFM, and FESEM analyses indicate the formation of a manganese nitrate nano-layer deposited on the SS304L substrate.
2. Analysis of polarization for investigation of the samples' resistance against corrosion in the 0.6 M NaCl solution at different temperatures showed that sample MnN_x(293 K)/SS304L had the lowest corrosion current density and the highest level of resistance against corrosion.
3. Results of EIS and Bode and Phase analyses revealed that MnN_x(293 K)/SS304L had the highest level of resistance while the lowest level of porosity.
4. Results of Kramers–Kronig transformations also confirmed the veracity of the data obtained from the other analyses.

It is therefore concluded that deposition of Mn on a SS304L substrate and annealing with nitrogen flux significantly improves the SS304L resistance to corrosion in a 0.6 M NaCl electrolyte at 293 K. Besides, due to the increased speed of reactions, raising the temperature of the solution reduces the resistance of the surface against corrosion. Moreover, grain boundaries, pores, and defects on the surface in sample MnN_x(293 K)/SS304L are reduced to the lowest level and this prevents the excessive penetration of the electrolyte into the metal. Therefore, the sample has shown the highest level of stability phase and resistance in this study.

References

1. Elanchezhian, C., Vijaya Ramnath, B., Ramakrishnan, G., Sripada Raghavendra, K.N., Muralidharan, M., Kishore, V.: Review on metal matrix composites for marine applications. Mater. Today Proc. **5**, 1211–1218 (2018)
2. Dirisu, J.O., Fayomi, O.S.I., Oyedepo, S.O., Jolayemi, K.J., Moboluwarin, D.M.: Critical evaluation of aluminium dross composites and other potential building ceiling materials. Procedia Manuf. **35**, 1205–1210 (2019)
3. Saravanan, C., Subramanian, K., Krishnan, V.A., Sankara Narayanan, R.: Effect of particulate reinforced aluminium metal matrix composite—a review. Mech. Mech. Eng. **19**, 23–30 (2015)
4. Abrahami, S.T., de Kok, J.M.M., Terryn, H., Mol, J.M.C.: Towards Cr(VI)-free anodization of aluminum alloys for aerospace adhesive bonding applications: a review. Front. Chem. Sci. Eng. **11**, 465–482 (2017)
5. Javidparvar, A.A., Ramezanzadeh, B., Ghasemi, E.: Effect of various spinel ferrite nanopigments modified by amino propyl trimethoxy silane on the corrosion inhibition properties of the epoxy nanocomposites. Corrosion **72**, 761–774 (2016)
6. Canepa, E., Stifanese, R., Merotto, L., Traverso, P.: Corrosion behaviour of aluminium alloys in deep-sea environment: a review and the KM3NeT test results. Mar. Struct. **59**, 271–284 (2018)
7. Fateh, A., Aliofkhazraei, M., Rezvanian, A.R.: Review of corrosive environments for copper and its corrosion inhibitors. Arab. J. Chem. **13**, 481–544 (2017)
8. Bodunrin, M.O., Alaneme, K.K., Chown, L.H.: Aluminium matrix hybrid composites: a review of reinforcement philosophies; mechanical, corrosion and tribological characteristics. J. Mater. Res. Technol. **4**, 434–445 (2015)
9. Javidparvar, A.A., Naderi, R., Ramezanzadeh, B.: Epoxy-polyamide nanocomposite coating with graphene oxide as cerium nanocontainer generating effective dual active/barrier corrosion protection. Compos. B Eng. **172**, 363–375 (2019)
10. Manam, N.S., Harun, W.S.W., Shri, D.N.A., Ghani, S.A.C., Kurniawan, T., Ismail, M.H., et al.: Study of corrosion in biocompatible metals for implants: a review. J. Alloy Compd. **701**, 698–715 (2017)
11. Corradi, M., Di Schino, A., Borri, A., Rufini, R.: A review of the use of stainless steel for masonry repair and reinforcement. Constr. Build. Mater. **181**, 335–346 (2018)
12. Lai, J.K.L.: A review of precipitation behaviour in AISI type 316 stainless steel. Mater. Sci. Eng. **61**, 101–109 (1983)
13. Davison, R.M., Laurin, T.R., Redmond, J.D., Watanabe, H., Semchyshen, M.: A review of worldwide developments in stainless steels. Mater. Des. **7**, 111–119 (1986)
14. Loto, R.T.: Pitting corrosion evaluation of austenitic stainless steel type 304 in acid chloride media (PDF Download Available). J. Mater. Environ. **4**, 448–459 (2013)
15. Sun, G.F., Zhang, Y.K., Zhang, M.K., Zhou, R., Wang, K., Liu, C.S., et al.: Microstructure and corrosion characteristics of 304 stainless steel laser-alloyed with Cr–CrB2. Appl. Surf. Sci. **295**, 94–107 (2014)
16. Loto, R.T.: Study of the corrosion resistance of type 304L and 316 austenitic stainless steels in acid chloride solution. Orient. J. Chem. **33**, 1090–1096 (2017)
17. Huang, C.A., Chang, Y.Z., Chen, S.C.: The electrochemical behavior of austenitic stainless steel with different degrees of sensitization in the transpassive potential region in 1 M H_2SO_4 containing chloride. Corros. Sci. **46**, 1501–1513 (2004)
18. Bankiewicz, D.: Corrosion behaviour of boiler tube materials during combustion of fuels containing Zn and Pb [Academic Dissertation]. Process Chemistry Centre, Department of Chemical Engineering, Abo Akademi University, Turku, Finland, Laboratory of Inoganic Chemistry (2012)
19. Baddoo, N.R.: Stainless steel in construction: a review of research, applications, challenges and opportunities. J. Constr. Steel Res. **64**, 1199–1206 (2008)
20. Agarwal, S., Suhane, A.: Study of boiler maintenance for enhanced reliability of system a review. Mater. Today Proc. **4**, 1542–1549 (2017)
21. Zhang, H., Zhao, Y.L., Jiang, Z.D.: Effects of temperature on the corrosion behavior of 13Cr martensitic stainless steel during exposure to CO_2 and Cl^- environment. Mater. Lett. **59**, 3370–3374 (2005)
22. Jian, L., Huanjun, Z., Ke, W., Xuehui, W.: Corrosion behavior of SS-304 in NaCl solution at different temperatures using electrochemical noise technique. Int. J. Electrochem. Sci. **10**, 931–937 (2015)

23. Masalski, J., Gluszek, J., Zabrzeski, J., Nitsch, K., Gluszek, P.: Improvement in corrosion resistance of the 316L stainless steel by means of Al2O3 coatings deposited by the sol–gel method. Thin Solid Films **349**, 186–190 (1999)
24. Shen, G.X., Chen, Y.C., Lin, C.J.: Corrosion protection of 316 L stainless steel by a TiO_2 nanoparticle coating prepared by sol–gel method. Thin Solid Films **489**, 130–136 (2005)
25. Li, M., Luo, S., Zeng, C., Shen, J., Lin, H., Cao, C.: Corrosion behavior of TiN coated type 316 stainless steel in simulated PEMFC environments. Corros. Sci. **46**, 1369–1380 (2004)
26. Javidparvar, A.A., Ramezanzade, B., Ghasemi, E.: The effect of oleic acid/silanetreatments of Fe_3O_4 nanoparticles on the mechanical properties of an epoxy coating, vol. 13, p. Dec. Institute for Color Scienceand Technology, Tehran (2015)
27. Zhang, X., Xiao, G., Jiang, C., Liu, B., Li, N., Zhu, R., et al.: Influence of process parameters on microstructure and corrosion properties of hopeite coating on stainless steel. Corros. Sci. **94**, 428–437 (2015)
28. Mohammadloo, H.E., Sarabi, A.A., Alvani, A.A.S., Salimi, R., Sameie, H.: The effect of solution temperature and pH on corrosion performance and morphology of nanoceramic-based conversion thin film. Mater. Corros. **64**, 535–543 (2013)
29. Chou, W.J., Yu, G.P., Huang, J.H.: Corrosion behavior of TiN-coated 304 stainless steel. Corros. Sci. **43**, 2023–2035 (2001)
30. Ćurković, L., Ćurković, H.O., Salopek, S., Renjo, M.M., Šegota, S.: Enhancement of corrosion protection of AISI 304 stainless steel by nanostructured sol–gel TiO_2 films. Corros. Sci. **77**, 176–184 (2013)
31. Mahdi Salih, S., Shakir, I.K., Al-Sammarraie, A.M.A.: Comparison of aggressiveness behavior of chloride and iodide solutions on 304 and 304L stainless steel alloys. Mater. Sci. Appl. **8**, 12 (2017)
32. Schönleber, M., Klotz, D., Ivers-Tiffée, E.: A method for improving the robustness of linear Kramers–Kronig validity tests. Electrochim. Acta **131**, 20–27 (2014)
33. Boukamp, B.A.: Practical application of the Kramers–Kronig transformation on impedance measurements in solid state electrochemistry. Solid State Ionics **62**, 131–141 (1993)
34. Khojier, K., Savaloni, H., Sadeghi, Z.: A comparative investigation on growth, nanostructure and electrical properties of copper oxide thin films as a function of annealing conditions. J Theor Appl Phys **8**, 116 (2014)
35. Modiri, F., Savaloni, H.: A study of the corrosion of stainless steel 304L coated with a 190 nm-thick manganese layer and annealed with nitrogen flux in a 0.4-mole solution of H_2SO_4 at different temperatures. J. Theor. Appl. Phys. **14**, 21–35 (2019)
36. Movchan, B.A., Demchishin, A.V.: Study of the structure and properties of thick vacuum condensates of nickel, titanium, tungsten, aluminium oxide and zirconium dioxide. Phys. Thin Film Met. Metall. **28**, 83 (1969)
37. Savaloni, H., Player, M.A., Gu, E., Marr, G.V.: Influence of substrate temperature, deposition rate, surface texture and material on the structure of uhv deposited erbium films. Vacuum **43**, 965–980 (1992)
38. Savaloni, H., Player, M.A.: Influence of deposition conditions and of substrate on the structure of uhv deposited erbium films. Vacuum **46**, 167–179 (1995)
39. Savaloni, H., Bagheri Najmi, S.: Characteristics of Cu and Zn films deposited on glass and stainless steel substrates at different substrate temperatures and angle of incidence. Vacuum **66**, 49–58 (2002)
40. Jonsson, T., Karlsson, S., Hooshyar, H., Sattari, M., Liske, J., Svensson, J.-E., Johansson, L.-G.: Oxidation after breakdown of the chromium-rich scale on stainless steels at high temperature: internal oxidation. Springer **85**, 509–536 (2016)
41. Jankowski, J., Juchniewicz, R.: A four-point method for corrosion rate determination. Corros. Sci. **20**, 841–851 (1980)
42. Rocchini, G.: Corrosion rate monitoring by the linear polarization method. Corros. Sci. **34**, 2031–2044 (1993)
43. Escrivà-Cerdána, C., Blasco-Tamarita, E., García-Garcíaa, D.M., García-Antón, J., Guenbourb, A.: Temperature effect on the austenitic stainless steel UNS N08031 used in the wet method phosphoric acid production. Chem. Eng. Trans. **32**, 1717–1722 (2013)
44. Blasco-Tamarit, E., Igual-Muñoz, A., García Antón, J., García-García, D.: Effect of temperature on the corrosion resistance and pitting behaviour of Alloy 31 in LiBr solutions. Corros. Sci. **50**, 1848–1857 (2008)
45. Rahmouni, K., Keddam, M., Srhiri, A., Takenouti, H.: Corrosion of copper in 3% NaCl solution polluted by solphide ions. Corros. Sci. **47**, 3249–3266 (2005)
46. Lei, Z., Zhanga, Q., Zhua, X., Maa, D., Maa, F., Songa, Z., Fub, Y.Q.: Corrosion performance of ZrN/ZrO_2 multilayer coatings deposited on 304 stainless steel using multi-arc ion plating. Appl. Surf. Sci. **431**, 170–176 (2018)
47. Al-Daraghmeha, M.Y., Hayajneha, M.T., Almomania, M.A.: Resistance of TiO_2–ZrO_2 nano-composite thin films spin coated on $AISI_3O_4$ stainless steel in 3.5 wt% NaCl solution. Mater. Res. **22**, e20190014 (2019)
48. Carvalho, J.B.R., Silva, R.S., Cesarino, I., Machado, S.A.S., Eguiluz, K.I.B., Cavalcanti, E.B., Salazar-Banda, G.R.: Influence of the annealing temperature and metal salt precursor on the structural characteristics and anti-corrosion barrier effect of CeO_2 sol–gel protective coatings of carbon steel. Ceram. Int. **40**, 13437–13446 (2014)
49. Poorqasemi, E., Abootalebi, O., Peikari, M., Haqdar, F.: Investigating accuracy of the Tafel extrapolation method in HCl solutions. Corros. Sci. **51**, 1043–1054 (2009)
50. Sorensen, P.A., Kiil, S., Dam-Johansen, K., Weinell, C.E.: Anticorrosive coatings: a review. J. Coat. Technol. Res. **6**, 135–176 (2009)
51. Fattah-alhosseini, A., Farahani, H.: Electrochemical behavior of AISI 304 stainless steel in sulfuric solution. J. Mater. Sci. Eng. **10**, 4 (2013)
52. Javidparvar, A.A., Ramezanzadeh, B., Ghasemi, E.: The effect of surface morphology and treatment of Fe_3O_4 nanoparticles on the corrosion resistance of epoxy coating. J. Taiwan Inst. Chem. Eng. **61**, 356–366 (2015)
53. Palomino, L.E.M., Aoki, I.V., de Melo, H.G.: Microstructural and electrochemical characterization of Ce conversion layers formed on Al alloy 2024–T3 covered with Cu-rich smut. Electrochim. Acta **51**, 5943–5953 (2006)
54. Yoganandan, G., Premkumar, K.P., Balaraju, J.: Evaluation of corrosion resistance and self-healing behavior of zirconium–cerium conversion coating developed on AA2024 alloy. Surf. Coat. Technol. **270**, 249–258 (2015)
55. Mahdavian, M., Attar, M.M.: Another approach in analysis of paint coatings with EIS measurement: phase angle at high frequencies. Corros. Sci. **48**, 4152–4157 (2006)
56. Hassanzadeh, A.: Validity of dynamic electrochemical impedance spectra of some amine corrosion inhibitors in petroleum/water corrosive mixtures by Kramers–Kronig transformation. Corros. Sci. **49**, 1895–1906 (2007)
57. Abdeli, M., Parvini Ahmadi, N., Azari Khosroshahi, R.: Influence of bis-(2-benzothiazolyl)-disulfide on corrosion inhibition of mild steel in hydrochloric acid media. J. Solid State Electrochem. **15**, 1867–1873 (2011)
58. Popkirov, G., Schindler, R.N.: A new approach to the problem of "good" and "bad" impedance data in electrochemical impedance spectroscopy. Electrochim. Acta **39**, 2025–2030 (1994)
59. Allen, J., Bard, L.R.F.: Electrochemical methods, fundamentals and applications. 2ndEdition (2001). ISBN: 978-471-04372-0
60. Zhang, J., Monteiro, P.J.M.: Validation of resistivity spectra from reinforced concrete corrosion by Kramers–Kronig transformations. Cem. Concr. Res. **31**, 603–607 (2001)
61. Achatz, G., Herzog, G.W., Plot, W.H.: Kramers–Kronig transformation of double-layer capacitances. Surf. Technol. **11**, 431–441 (1980)

62. Javidparvar, A.A., Naderi, R., Ramezanzadeh, B.: Manipulating graphene oxide nanocontainer with benzimidazole and cerium ions: application in epoxy-based nanocomposite for active corrosion protection. Corros. Sci. **165**, 108379 (2020)

Publisher's Note Springer Nature remains neutral with regard to jurisdictional claims in published maps and institutional affiliations.